



Article

Estimating Thermal Material Properties Using Step-Heating Thermography Methods in a Solar Loading Thermography Setup

Samuel Klein ^{1,*} , Tobias Heib ¹ and Hans-Georg Herrmann ^{1,2} 

¹ Chair for Lightweight Systems, Saarland University, Campus E3 1, 66123 Saarbrücken, Germany; tobias.heib@uni-saarland.de (T.H.); hans-georg.herrmann@izfp.fraunhofer.de (H.-G.H.)

² Fraunhofer Institute for Nondestructive Testing IZFP, Campus E3 1, 66123 Saarbrücken, Germany

* Correspondence: samuel.klein@uni-saarland.de

Featured Application: Exploring step-heating thermography algorithms applied to solar loading thermography.

Abstract: This work investigates solar loading thermography applications using active thermography algorithms. It is shown that active thermography methods, such as step-heating thermography, present good correlation with a solar loading setup. Solar loading thermography is an approach that has recently gained scientific attention and is advantageous because it is particularly easy to set up and can measure large-scale objects, as the sun is the primary heat source. This work also introduces the concept of using a pyranometer as a reference for the evaluation algorithms by providing a direct solar irradiance measurement. Furthermore, a recently introduced method of estimating thermal effusivity is evaluated on ambient-derived thermograms.

Keywords: solar loading thermography; step-heating thermography; active thermography; thermal effusivity; linear effusivity fit; infrastructure; NDT



Citation: Klein, S.; Heib, T.; Herrmann, H.-G. Estimating Thermal Material Properties Using Step-Heating Thermography Methods in a Solar Loading Thermography Setup. *Appl. Sci.* **2021**, *11*, 7456. <https://doi.org/10.3390/app11167456>

Academic Editor: Jerzy Hola

Received: 26 July 2021

Accepted: 10 August 2021

Published: 13 August 2021

Publisher's Note: MDPI stays neutral with regard to jurisdictional claims in published maps and institutional affiliations.



Copyright: © 2021 by the authors. Licensee MDPI, Basel, Switzerland. This article is an open access article distributed under the terms and conditions of the Creative Commons Attribution (CC BY) license (<https://creativecommons.org/licenses/by/4.0/>).

1. Introduction

Solar loading thermography has gained recent scientific attention [1–4] and shows the potential to become a proven non-destructive testing (NDT) method for large-scale outdoor structures and infrastructure. As natural heat sources are inherently erratic (affected by cloud coverage, wind gusts and ambient temperature fluctuations), evaluation algorithms must be reviewed on a case-by-case basis. The range of evaluation algorithms discussed in this work is constrained to conventional active thermography approaches, namely, lock-in thermography (LIT) [5], step-heating thermography (SHT) [6] and linear effusivity fit (LEF) [7]. Each of these may be used to determine thermal material properties, in this case, the thermal effusivity of an excited object. Thermal effusivity is a measure of how strongly a material exchanges heat with its surroundings: higher effusivity means a slower response to heat input, whereas lower effusivity means a quicker response. Thermal effusivity is also the main reason why different materials feel cold or hot to the touch, despite being at the same temperature initially.

Determining thermal effusivity using solar loading lock-in thermography was shown in our previous work [1], but empirical calibration was needed to do so. In this work, we propose an alternative approach using a pyranometer to measure the insolation (solar irradiance) directly. This allows the experimenter to directly assess the irradiation shape and amplitude at each point in time, which, in turn, allows the creation of analogies to conventional, laboratory-scale active thermography methods.

2. Materials and Methods

This work used a pyranometer to measure insolation. The model used was an “LP PYRA 03” from Delta Ohm (Padua, Italy), This model is a second-class pyranometer, which means that it satisfies the ISO 9060 Second-class accuracy class definition. It is connected to the measurement card consisting of the ADS1256 ADC, which has sufficient accuracy and resolution to digitize the signal generated by the pyranometer appropriately.

A custom data acquisition platform was developed, powered by a rechargeable battery and consisting of an embedded Linux single board computer (RaspberryPi 3B) and the FLIR Boson 640 in USB Video (UVC) mode. The FLIR long wave infrared (LWIR) thermal imaging camera, which can directly send raw image data over USB, was used in all further processing. This camera is sensitive between 7.5 μm and 13.5 μm .

The camera was calibrated once within the approximated expected temperature range using a large-aperture blackbody source (Mikron M345X4). All thermograms were corrected using a two-point calibration scheme based on a radiometric calibration. All algorithms and figures were created using the free software “GNU Octave” and commercial software “MATLAB”.

3. Theoretical Framework

Solar loading lock-in thermography does not use artificial heat sources, such as heat lamps; its only heat processes are naturally occurring. These consist of the following: heat transfer within the structure (conduction); heat transfer with the surrounding air, which is free to move (convection); and heat transfer via radiation (solar irradiation, radiative heat loss). The fourth heat process, evaporative cooling, was not included in this study.

To estimate thermal material properties, the value of the heat flux input is needed. Therefore, a direct measurement of the insolation was conducted using a pyranometer.

As described in our previous work [1], the infrared camera was set up in a stationary position to capture a set of thermal images regularly spaced in time. These images represented a 2D temperature field that was assumed to capture the surface temperature of a structure after radiance calibration with a blackbody source. Effects such as emissivity/reflectivity can be corrected to improve absolute measuring accuracy for a given surface. These kinds of corrections were not performed in the scope of this work but are hypothesized to further increase measurement accuracy in future research [1].

The pyranometer was fixed horizontally, effectively measuring global horizontal irradiation (GHI). As different captured structures faced different angles, a correction from GHI to the respective vertical angle surfaces was conducted. This correction was performed via a two-step process:

1. Calculate the theoretical values for direct horizontal irradiation (DHI) and direct vertical irradiation (DVI) at the angle of interest.
2. Correct the pyranometer GHI data using the factor DVI/DHI .

The correction can be found in Figure 1.

Both DHI and DVI can be determined using the air mass coefficient method [8], where DVI must be calculated for each angle of interest (e.g., 180° = facing south, 225° = facing south west).

For horizontally oriented surfaces, no correction to the pyranometer data was necessary, as they were recorded horizontally.

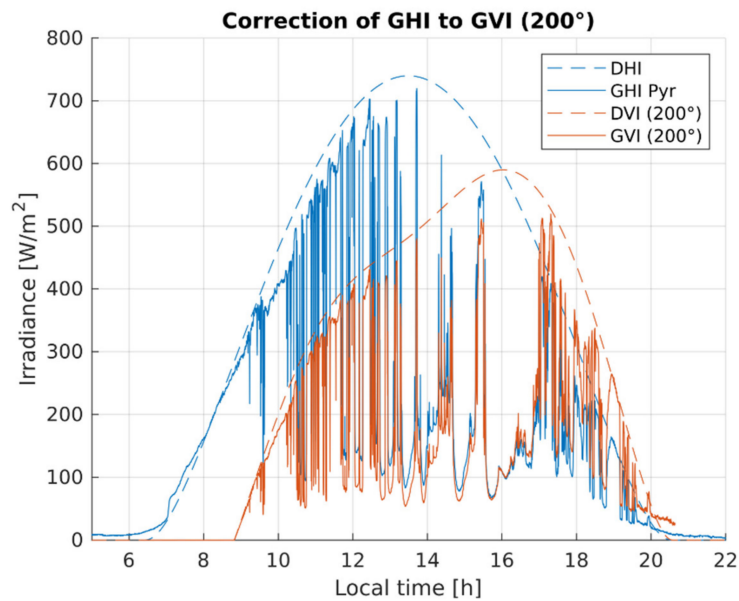


Figure 1. Correction of GHI to GVI on a 200° facing angle. Note that the theoretical values for DHI and DVI were calculated according to [8] and were used to correct the measured GHI data to infer the irradiance on the vertical standing wall structures (GVI).

After correction of the irradiation value, multiple approaches from active thermography to determine thermal material properties were evaluated:

1. Determining thermal effusivity b via step-heating thermography approach [6];
2. Determining thermal effusivity b via linear effusivity fit approach [7];
3. Determining surface heat capacity c_S [9].

The results of these three methods are discussed in the next section.

3.1. SHT Approach

According to [6], the temperature rise of thermally thick sample is given by

$$\Delta T = 2\dot{q} \cdot \sqrt{\frac{t}{\pi \cdot \lambda c_P \rho}} \quad (1)$$

where \dot{q} is the step heating irradiation in $[\text{W}/\text{m}^2]$, t the irradiation time, λ the heat conductivity in $[\text{W}/\text{mK}]$, c_P the specific heat in $[\text{J}/\text{kg}]$ and ρ the density of the material in $[\text{kg}/\text{m}^3]$.

Considering the thermal effusivity, which is given by:

$$b = \sqrt{\lambda c_P \rho} \quad (2)$$

The formula can be rewritten as:

$$b = \frac{2\dot{q}}{\Delta T} \cdot \sqrt{\frac{t}{\pi}} \quad (3)$$

This formula calculates the thermal effusivity in a step-heating context on thermally thick materials (materials where the thermal wave can properly develop and travel without reflecting). Generally, thermally thick materials have a thickness $d \gg \mu$, where μ is the thermal diffusion length in $[\text{m}]$. The thermal diffusion length is given by:

$$\mu = \sqrt{\frac{2\lambda}{\rho c_P \cdot \omega}} \quad (4)$$

where ω is the angular frequency of the incident thermal wave in $[\text{s}^{-1}]$.

In this work, the angular frequency of the step-heating pulse was determined using $\omega = \pi/t$. In practice, objects with a thickness of $d > 1.5\mu$ show negligible error when considered thermally thick [6]. This cutoff value of 1.5μ is not universally applicable and was only used in this context because it generated reasonable results. In other setups with different excitation conditions and materials, other values distinguishing thermally thick from thermally thin materials may be necessary.

3.2. Surface Heat Capacity (SHC) Approach

Contrary to thermally thick materials, thermal “thinness” can be assumed when $d < 0.5\mu$. Again, the same restrictions as above apply to this empirically generated value.

When measuring a thermally thin object, thermal effusivity is not a valid material property to determine, because the formulas calculating it consider the material to be fully extended as a half space (infinitely thermally thick). Instead, surface heat capacity c_S in $[\text{J}/(\text{m}^2\text{K})]$ can be calculated and used to determine one of three values (ρ , c_P or d) when the other two are either known or assumed.

The surface heat capacity is defined as the ratio of the radiant exposure q in $[\text{J}/\text{m}^2]$ and the resulting temperature difference ΔT :

$$c_S = \frac{q}{\Delta T} \quad (5)$$

The radiant exposure of a step is the product of the heat flux density \dot{q} and the corresponding effective time t and leads to:

$$c_S = t \cdot \frac{\dot{q}}{\Delta T} \quad (6)$$

In thermally thin materials, the surface heat capacity can be derived from the volumetric heat capacity s , as thermally thin materials act as if the heat spreads instantly in the direction of their thickness. In this case, c_S can also be determined via:

$$c_S = \overbrace{\rho c_P}^s \cdot d \quad (7)$$

This allows the determination of ρ , c_P or d if both other values are either known or assumed.

3.3. LEF Approach

The linear effusivity fit is a method introduced by Suchan and Hendorfer [7], using the Laplace transform to transform both the irradiation pulse and the temperature response from the surface into the frequency domain to determine the thermal effusivity by fitting a linear function to the quotient of the transformed data. It can be briefly described as a four-step process:

1. Transform both irradiation pulse $q(t)$ and surface temperature $T(t)$ using the discrete Laplace transform into the complex frequency domain to obtain $\bar{q}(s)$ and $\bar{T}(s)$, respectively. Note that s denotes the complex Laplace operator value.
2. Calculate the quotient of the aforementioned signals:

$$\bar{Z}(s) = \frac{\bar{T}(s)}{\bar{q}(s)} \quad (8)$$

3. Thermal effusivity is given by:

$$\bar{Z}(s) = \frac{1}{b \cdot \sqrt{s}} \quad (9)$$

Plotting $\bar{Z}(s)$ over $(\sqrt{s})^{-1}$ results in a linear relationship: $\bar{Z}(s)/\sqrt{s} = b^{-1}$, the slope m of this function being b^{-1} .

4. A linear fit using $\bar{Z}(s)$ over $(\sqrt{s})^{-1}$ is performed and the slope of this fit is inverted to obtain

$$b = 1/m_{Fit} \quad (10)$$

The linear fit is necessary to suppress noise and high-frequency content in the resulting transformed values, but in theory, two points from $\bar{Z}(s)$ could be used to determine b .

This approach was employed in a region of interest-based context, where a single region of interest (ROI) was given as a mean value time vector to the algorithm to calculate the material properties of the whole ROI. Further, it was conducted on a pixel basis, where the LEF method was performed on each pixel to obtain an “effusivity image”.

3.4. Albedo Factor and Surface Emissivity

Figure 2 shows that the heating step had an amplitude of $\sim 320 \text{ W/m}^2$ for horizontal surfaces and $\sim 300 \text{ W/m}^2$ for vertical surfaces at 200° . These values represent the total amount of incident radiation. However, as every surface absorbed only a part of the incoming energy (called the emissivity factor), this irradiation was only absorbed by blackbodies. As incident radiation energy (sunlight) is primarily visual and near infrared (NIR) energy [10], the factor used in this work to refer to the amount of reflected sunlight was albedo α , and the term describing the energy factor absorbed (and emitted) in the LWIR range was determined as emissivity ε .

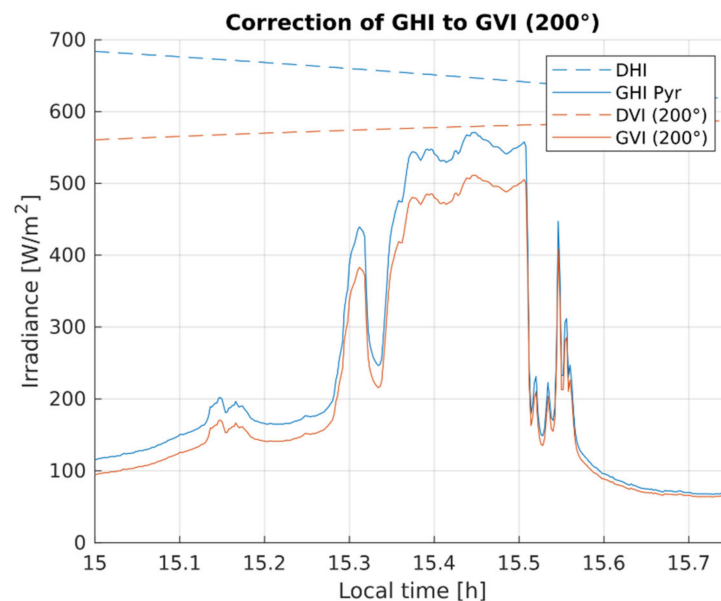


Figure 2. Correction of GHI to GVI as before, zoomed in to show the relevant part of the dataset containing step heating.

As the albedo of white plaster is approximately ~ 0.65 [11], the actual absorbed energy is 35% of the total incident irradiation. On grey surfaces, the albedo is ~ 0.55 [11], which results in an energy absorption of 45%. The albedo of grey pavement is ~ 0.60 [11].

As common building materials such as plaster and concrete are considered to have high emissivity (≥ 0.95) in the LWIR range [12] p. 316, an emissivity correction for the LWIR camera was not performed. Instead, the factors researched imposed an albedo correction first.

For Table 1 and all corrected figures, the albedo correction was performed using the aforementioned values.

The scene in Figure 3 shows the composition of a common street with houses, garages, trees, a car and a paved road. Due to this composition, not all of the four selected regions

of interest are perpendicular to the optical axis of the thermography camera. For further inspections, it was necessary to perform a projective transformation from the observed angle to a plane that is perpendicular to the optical axis. For the creation of the transformation matrix, two assumptions were made. First, it was assumed that the observed ROIs were flat surfaces, and second, the two building walls and the garage sidewall in particular had a rectangular shape. For each ROI, the four edge points of the studied object were selected and registered to a rectangular geometry with the aspect ratio of the observed object [13]. The projective mapping was carried out with MATLAB, using the “image processing toolbox”. Figure 4 shows a typical thermogram of the scene, with an overview over the ROIs chosen.



Figure 3. Optical overview over the scene.

Table 1. Overview of the different estimations. Note this table corrects for the albedo factor of the different image parts.
[†] The reference values are taken from [14–16] [‡] as the concrete road lay horizontally. GHI is the excitation intensity (see Figure 2).

	Temperature		Excitation Intensity	Surface Heat Capacity	Effusivity		
	Difference	Gradient			SHT	LEF	Reference [†]
Region of interest	K	K/min	W/m ²	kJ/(Km ²)	J/(Km ² √s)		
(1) Wall left	7	0.6	300	6	324	1024	490–780
(2) Wall right	5	0.4	300	14	454	1061	490–780
(3) Concrete road	4	0.3	320 [‡]	27	2132	1971	1730–2120
(4) Garage	3	0.25	300	19	1362	1581	1100–1400

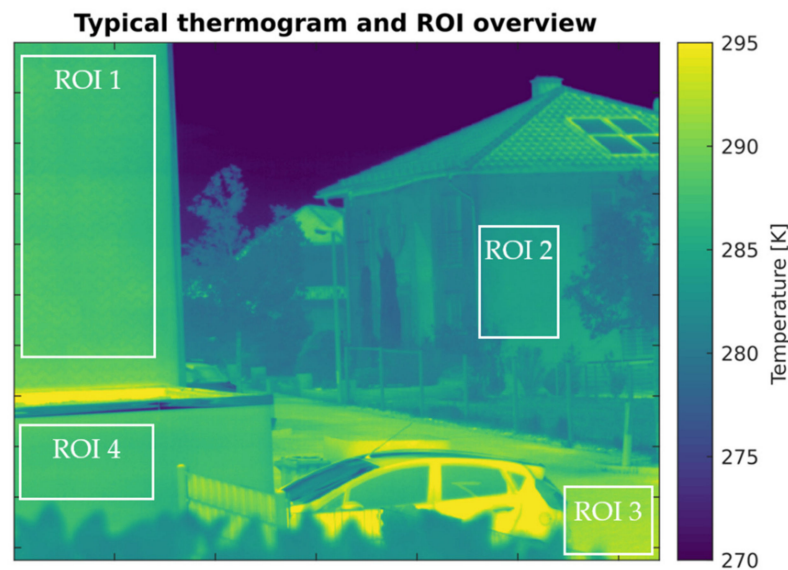


Figure 4. Typical thermogram of the scene with the selected ROIs of the experiment. ROI 1 is the left building wall, ROI 2 the right building wall, ROI 3 is the paved road, and ROI 4 the garage sidewall.

4. Results and Discussion

The experiment site was set up by measuring two building walls, a concrete-paved road and a garage sidewall. The general setup of the scene can be observed in Figure 3. The pyranometer data are shown in Figure 1 and constitute an excerpt from a much larger dataset, which was acquired over multiple days. However, for this work, the aforementioned algorithms required only a small portion of the whole dataset. Figure 2 shows the data section that is used in this work.

Figure 2 shows the relevant section from 15:00 h to 15:45 h with approximate step heating, generated by variation in cloud coverage. The blue curve (GHI) shows the irradiance incident to all horizontal surfaces in the scene, in this case, predominantly the paved road (ROI 3). The orange curve (GVI) was calculated from the GHI data to represent the incident irradiance on all 200° facing vertical structures, such as the two building sidewalls (ROI 1 and ROI 2) and the garage wall (ROI 4) shown in Figure 3. This explains the difference between the excitation intensities in Table 1.

Figure 5 was generated using a pixel-wise subtraction of the last image in the heating phase with the first image thereof. Note the uneven heating on the building on the right due to shadows being cast by the roof onto the wall below. This difference image was the basis for both the SHT effusivity estimation and SHC images below.

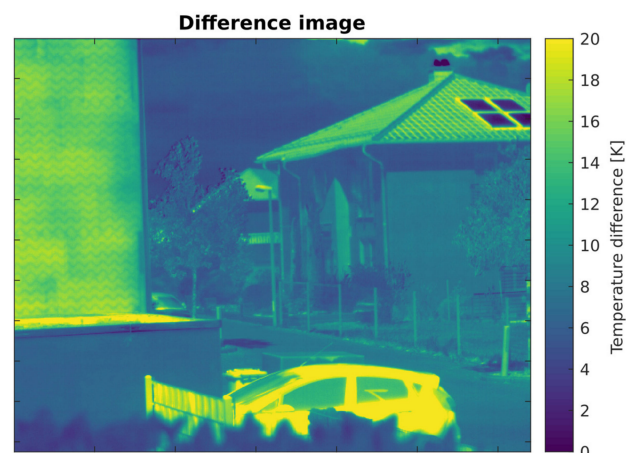


Figure 5. Difference image: last image in the heating phase subtracted by the first image thereof.

Figure 6 shows the uncorrected thermal effusivity. The shown image assumes a heat flux of 320 W/m^2 for all surfaces, but the real heat flux (albedo correction) must be estimated on a case-by-case basis to obtain correct estimates of thermal effusivity.

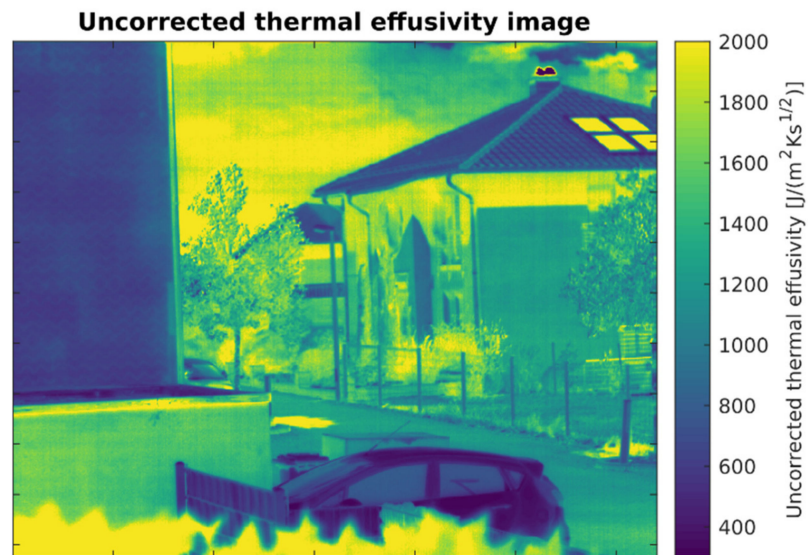


Figure 6. Effusivity image resulting from the SHT approach.

Figure 7 shows the uncorrected heat capacity, neglecting the albedo factor of the objects in the scene. The real surface heat capacity was reduced by a factor of $(1 - \alpha)$.

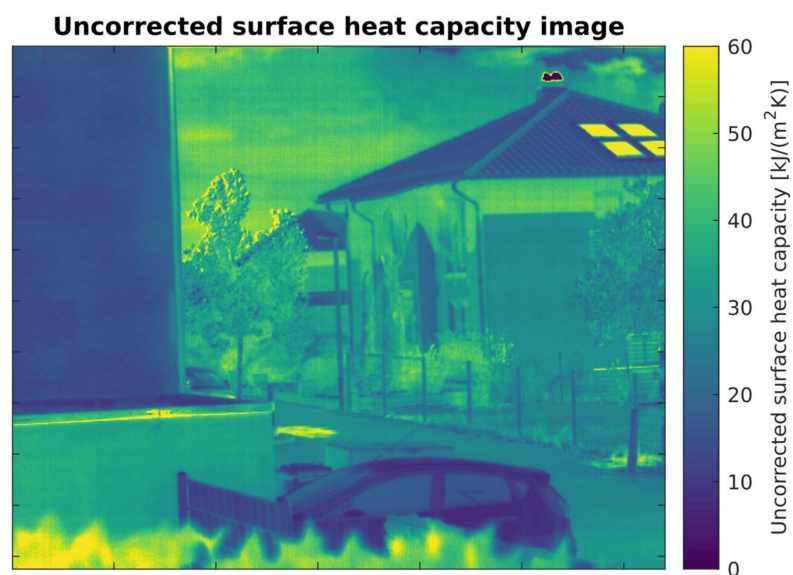


Figure 7. Surface heat capacity image.

The LEF algorithm was performed on each pixel of Figure 8 separately. Note that as before, no albedo correction was performed on this image, and each pixel was assumed to have absorbed the full incident irradiation.

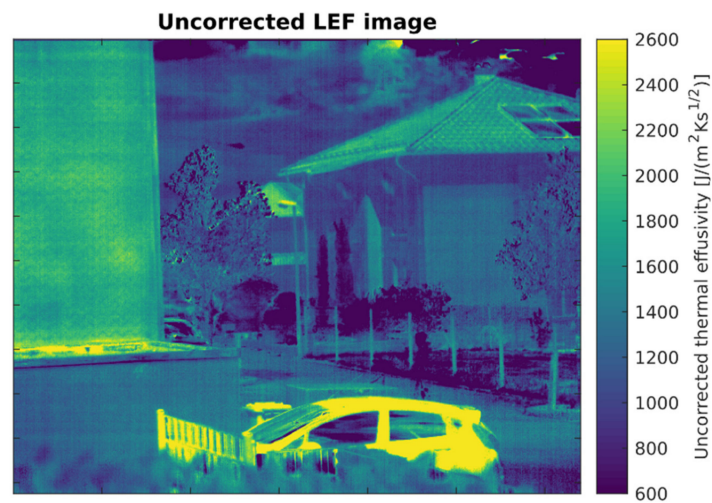


Figure 8. Linear effusivity fit image.

Note that this effusivity image (see Figure 8) differs from the image generated by the SHT effusivity estimation method (see Figure 6). This is, in part, because the underlying algorithm to determine surface effusivity by LEF was noise sensitive [7], and reducing noise by averaging a whole ROI delivered more reasonable values.

Table 1 summarizes the results of the different methods for the observed ROIs.

The garage wall consisted of hollow concrete blocks covered with a layer of gypsum. The two building walls consisted of an unknown type of insulating gypsum covering a conventional building insulation material, such as mineral wool or polystyrene.

Separating ROIs and correcting the trapezoidal distortion generated by the camera viewing each ROI surface from an angle helped to improve the visual clarity of the image. The results with separation and perspective correction are shown in Figures 9–12. Especially noteworthy are the following distinctive features:

- Wave-like structure in ROI 1—possible remnant of the insulation installation;
- Hot spot in the top middle of the garage (ROI 4);
- Apparent recognition of the floor in ROI 2.

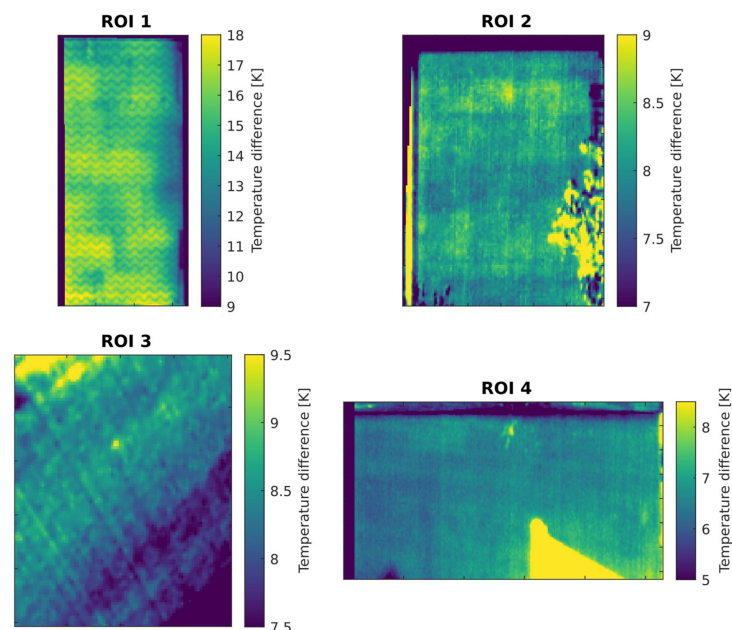


Figure 9. Perspective-corrected difference images.

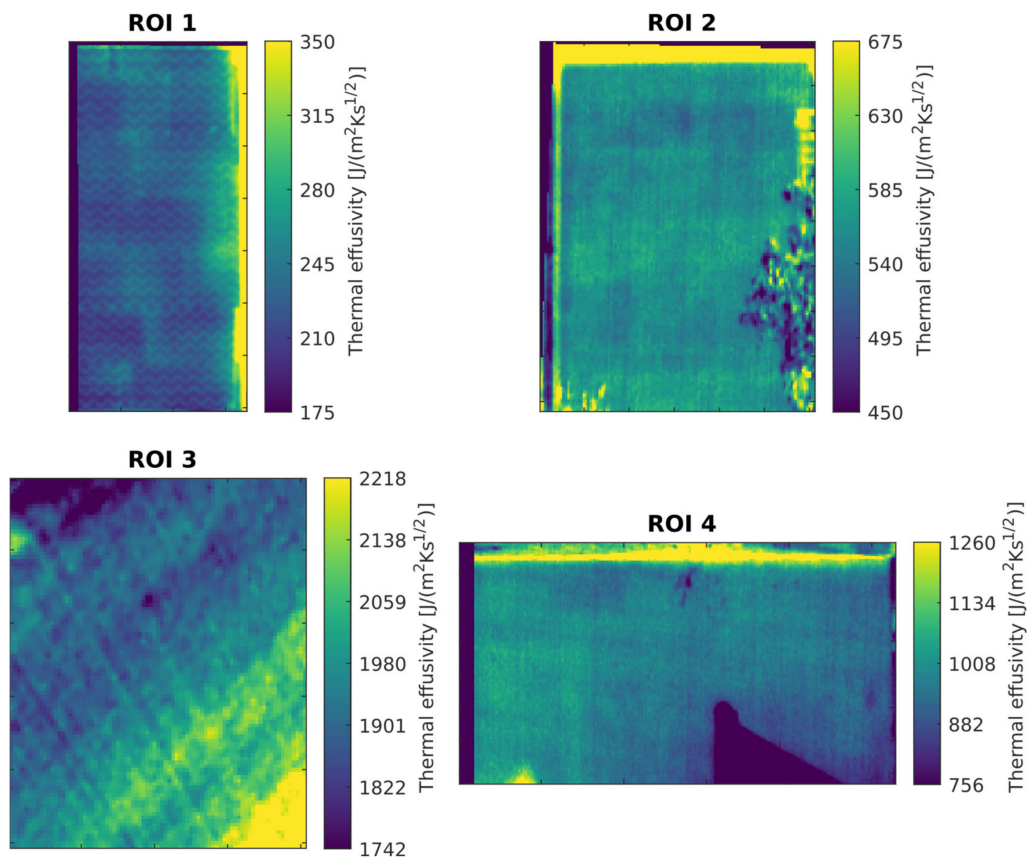


Figure 10. Perspective- and albedo-corrected SHT effusivity images.

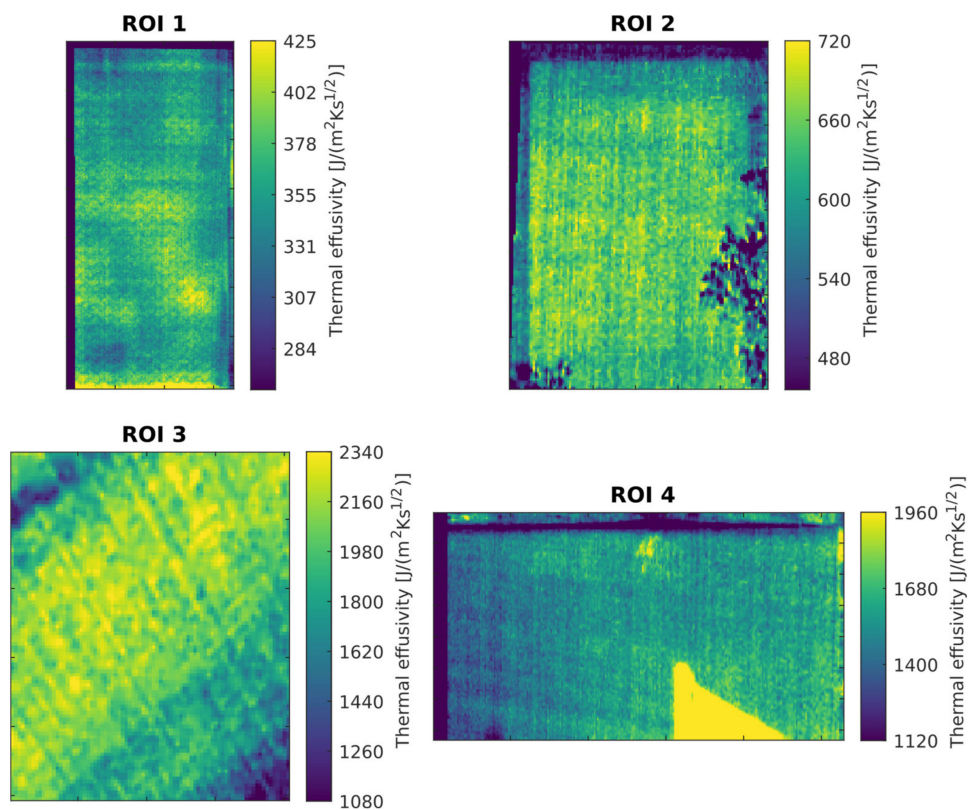


Figure 11. Perspective- and albedo-corrected LEF effusivity images.

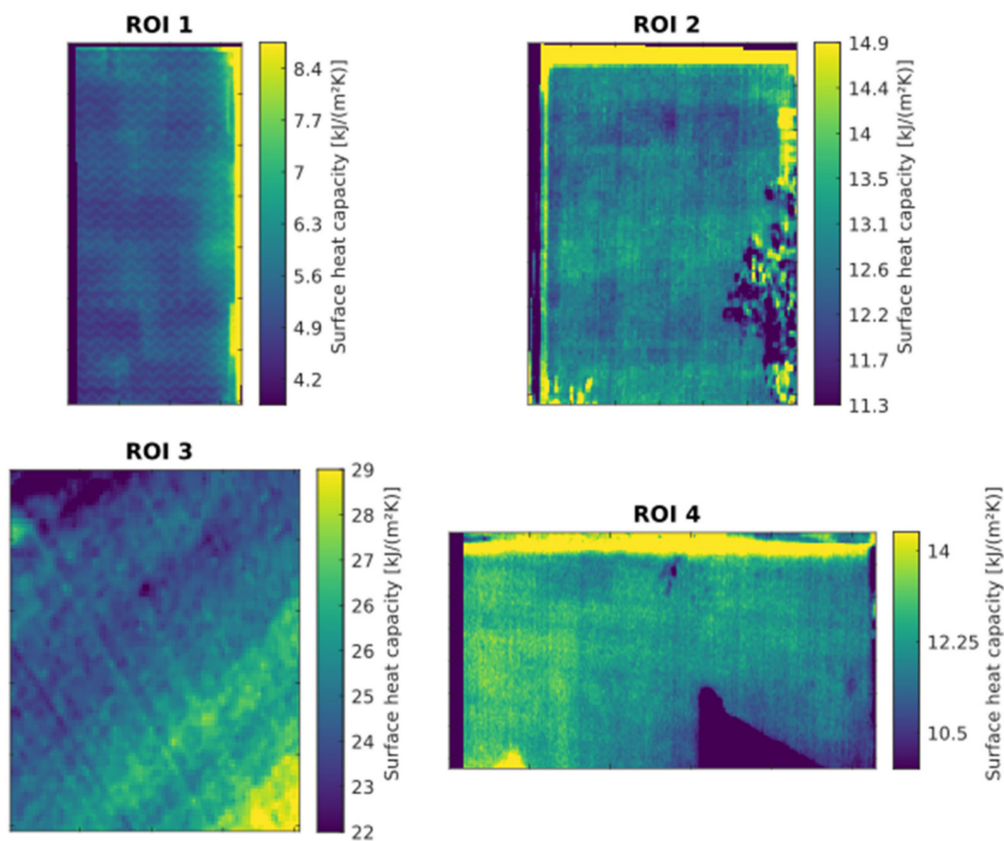


Figure 12. Perspective- and albedo-corrected surface heat capacity images.

5. Conclusions and Further Work

This study demonstrated that the methods used by laboratory-scale active thermography can be evaluated on solar loading thermograms. Depending on location conditions, such as weather and cloud coverage, both strong and weak resemblances to different testing methodologies, such as lock-in or step-heating thermography, can be observed. In general, signal-to-noise ratio is satisfactory in a solar loaded context, but the erratic excitation conditions, such as fluctuating irradiation and changing wind speeds, hamper the accuracy of the previously established assumptions made by the evaluation algorithms.

It was found that ideally, the experimental setup should record the region of interest perpendicularly in the first place. As this is not feasible in every experiment, separating ROIs from the whole image and correcting the perspective error can improve the apparent contrast and enhance visual clarity on the images.

Further work should evaluate how to take into account the given environmental conditions to better fit a specific test cast. For example, manual shading of a particular ROI may generate a step-heating scenario in strong sunlit conditions without the need for specific cloud coverage. Wind speed and ambient temperature could also be measured and evaluated to calculate the heat flow of the specific structures at all points in the experiment. However, specific algorithms and methods must be devised to correct the influences of these unpredictable factors.

Author Contributions: Conceptualization, S.K. and H.-G.H.; methodology, S.K.; software, S.K. and T.H.; validation, S.K. and H.-G.H.; writing—original draft preparation, S.K.; writing—review and editing, S.K., T.H. and H.-G.H.; visualization, S.K.; supervision, H.-G.H.; project administration, H.-G.H.; funding acquisition, H.-G.H. All authors have read and agreed to the published version of the manuscript.

Funding: The European Regional Development Fund (ERDF), especially grant number 14.2.1.4-2016-1, funded this research. Furthermore, we acknowledge support of the Deutsche Forschungsgemeinschaft (DFG, German Research Foundation) and Saarland University within the funding program Open Access Publishing.

Institutional Review Board Statement: Not applicable.

Informed Consent Statement: Not applicable.

Acknowledgments: Gratitude goes to Josef Suchan and Günther Hendorfer for excellent practice in scientific exchange. Furthermore, the authors thank Jessica Jacob for her help with experimental setup and conduction.

Conflicts of Interest: The authors declare no conflict of interest. The funders had no role in the design of the study; in the collection, analyses, or interpretation of data; in the writing of the manuscript; or in the decision to publish the results.

References

1. Klein, S.; Fernandes, H.; Herrmann, H.-G. Estimating thermal material properties using solar loading lock-in thermography. *Appl. Sci.* **2021**, *11*, 3097. [CrossRef]
2. Tu, K.; Ibarra-Castanedo, C.; Sfarra, S.; Yao, Y.; Maldague, X.P.V. Multiscale analysis of solar loading thermographic signals for wall structure inspection. *Sensors* **2021**, *21*, 2806. [CrossRef] [PubMed]
3. Ibarra-Castanedo, C.; Sfarra, S.; Klein, M.; Maldague, X. Solar loading thermography: Time-lapsed thermographic survey and advanced thermographic signal processing for the inspection of civil engineering and cultural heritage structures. *Infrared Phys. Technol.* **2017**, *82*, 56–74. [CrossRef]
4. Bagavathiappan, S.; Lahiri, B.B.; Saravanan, T.; Philip, J.; Jayakumar, T. Infrared thermography for condition monitoring—A review. *Infrared Phys. Technol.* **2013**, *60*, 35–55. [CrossRef]
5. Breitenstein, O.; Warta, W.; Langenkamp, M. *Lock-in Thermography*; Springer: Berlin/Heidelberg, Germany, 2010; ISBN 978-3-642-02416-0.
6. Boué, C.; Fournier, D. Infrared thermography measurement of the thermal parameters (effusivity, diffusivity and conductivity) of materials. *Quant. InfraRed Thermogr. J.* **2009**, *6*, 175–188. [CrossRef]
7. Suchan, J.; Hendorfer, G. Thermal effusivity determination of carbon fibre-reinforced polymers by means of active thermography. *Quant. InfraRed Thermogr. J.* **2020**, *17*, 210–222. [CrossRef]
8. Meinel, A.B.; Meinel, M.P. *Applied Solar Energy: An Introduction*; Addison-Wesley Publishing Company: Reading, MA, USA; New York, NY, USA, 1977; ISBN 9780201047196.
9. Logvinov, G.N.; Gurevich, Y.G.; Lashkevich, I.M. Surface heat capacity and surface heat impedance: An application to theory of thermal waves. *Jpn. J. Appl. Phys.* **2003**, *42*, 4448. [CrossRef]
10. Department of Agronomy, Iowa State University. Thermal Energy-Radiation Spectrum. Available online: <http://agron-www.agron.iastate.edu/courses/Agron541/classes/541/lesson09a/9a.3.html> (accessed on 1 July 2021).
11. Reagan, J.A.; Acklam, D.M. Solar reflectivity of common building materials and its influence on the roof heat gain of typical southwestern U.S.A. residences. *Energy Build.* **1979**, *2*, 237–248. [CrossRef]
12. Vavilov, V.; Burleigh, D. *Infrared Thermography and Thermal Nondestructive Testing*; Springer International Publishing: Cham, Germany, 2020; ISBN 978-3-030-48001-1.
13. Heckbert, P. Fundamentals of Texture Mapping and Image Warping. Master's Thesis, Berkeley University, Berkeley, CA, USA, 1989.
14. John, H.; Lienhard, I.V. *A Heat Transfer Textbook*, 5th ed.; Phlogiston Press: Cambridge, MA, USA, 2020.
15. Ouakarrouch, M.; Azhary, K.E.; Laaroussi, N.; Garoum, M. Thermal Performances of Hollow Concrete Blocks based on ISO Norm Calculations. In *Thermal Performances of Hollow Concrete Blocks based on ISO Norm Calculations*; IEEE: Piscataway, NJ, USA, 2019; ISBN 978-1-7281-5152-6.
16. American Society of Heating, Refrigerating and Air-Conditioning Engineers. In *2017 ASHRAE Handbook: Fundamentals*; ASHRAE: Atlanta, GA, USA, 2017; ISBN 9781939200570.